

## Article

# One-Pot Synthesis of SnO<sub>2</sub>-rGO Nanocomposite for Enhanced Photocatalytic and Anticancer Activity

ZabnAllah M. Alaizeri, Hisham A. Alhadlaq , Saad Aldawood , Mohd Javed Akhtar   
and Maqsood Ahamed\* 

Department of Physics and Astronomy, College of Sciences, King Saud University, Riyadh 11451, Saudi Arabia; zalaizeri@ksu.edu.sa (Z.M.A.); hhadlaq@ksu.edu.sa (H.A.A.); sdawood@ksu.edu.sa (S.A.); mjakhtar@ksu.edu.sa (M.J.A.)

\* Correspondence: mahamed@ksu.edu.sa

**Abstract:** Metal oxide and graphene derivative-based nanocomposites (NCs) are attractive to the fields of environmental remediation, optics, and cancer therapy owing to their remarkable physico-chemical characteristics. There is limited information on the environmental and biomedical applications of tin oxide-reduced graphene oxide nanocomposites (SnO<sub>2</sub>-rGO NCs). The goal of this work was to explore the photocatalytic activity and anticancer efficacy of SnO<sub>2</sub>-rGO NCs. Pure SnO<sub>2</sub> NPs and SnO<sub>2</sub>-rGO NCs were prepared using the one-pot hydrothermal method. X-ray diffraction (XRD), transmission electron microscopy (TEM), scanning electron microscopy (SEM), X-ray photoelectron spectroscopy (XPS), Fourier transform infrared (FTIR), UV-Vis spectrometry, photoluminescence (PL), and Raman scattering microscopy were applied to characterize the synthesized samples. The crystallite size of the SnO<sub>2</sub> NPs slightly increased after rGO doping. TEM and SEM images show that the SnO<sub>2</sub> NPs were tightly anchored onto the rGO sheets. The XPS and EDX data confirmed the chemical state and elemental composition of the SnO<sub>2</sub>-rGO NCs. Optical data suggest that the bandgap energy of the SnO<sub>2</sub>-rGO NCs was slightly lower than for the pure SnO<sub>2</sub> NPs. In comparison to pure SnO<sub>2</sub> NPs, the intensity of the PL spectra of the SnO<sub>2</sub>-rGO NCs was lower, indicating the decrement of the recombination rate of the surfaces charges (e<sup>-</sup>/h<sup>+</sup>) after rGO doping. Hence, the degradation efficiency of methylene blue (MB) dye by SnO<sub>2</sub>-rGO NCs (93%) was almost 2-fold higher than for pure SnO<sub>2</sub> NPs (54%). The anticancer efficacy of SnO<sub>2</sub>-rGO NCs was also almost 1.5-fold higher against human liver cancer (HepG2) and human lung cancer (A549) cells compared to the SnO<sub>2</sub> NPs. This study suggests a unique method to improve the photocatalytic activity and anticancer efficacy of SnO<sub>2</sub> NPs by fusion with graphene derivatives.



**Citation:** Alaizeri, Z.M.; Alhadlaq, H.A.; Aldawood, S.; Akhtar, M.J.; Ahamed, M. One-Pot Synthesis of SnO<sub>2</sub>-rGO Nanocomposite for Enhanced Photocatalytic and Anticancer Activity. *Polymers* **2022**, *14*, 2036. <https://doi.org/10.3390/polym14102036>

Academic Editor: Sidi A. Bencherif

Received: 3 April 2022

Accepted: 13 May 2022

Published: 16 May 2022

**Publisher's Note:** MDPI stays neutral with regard to jurisdictional claims in published maps and institutional affiliations.



**Copyright:** © 2022 by the authors. Licensee MDPI, Basel, Switzerland. This article is an open access article distributed under the terms and conditions of the Creative Commons Attribution (CC BY) license (<https://creativecommons.org/licenses/by/4.0/>).

**Keywords:** SnO<sub>2</sub>; rGO; nanocomposites; one-pot synthesis; characterization; photocatalytic degradation; anticancer activity

## 1. Introduction

Hepatocellular carcinoma is the second leading cause of death after lung cancer, globally [1]. The World Health Organization (WHO) reported that there were approximately 19 million new cancer cases and approximately 10 million deaths from cancer worldwide in 2020 [2]. There are several ways, such as surgery, radiation, and chemotherapy, to treat cancer. However, drug resistance and selectivity are still two major hurdles in cancer therapy. On the other hand, the release of environmental pollutants (e.g., dyes and drugs) from various factories challenge the intactness of the ecosystem. Hence, it is important to develop a nanostructure that can be used in biomedical as well as environmental applications [3].

Metal nanoparticles, such as silver nanoparticles (AgNPs), have recently become attractive to different areas such as catalysis, bio-sensing, antimicrobial activity, and biomedicine due to the fact of their potential applications [4,5]. Metal oxide nanoparticles (NPs) have shown potential for their application in cancer therapy and environmental

remediation [6,7]. For example, NPs of ZnO, TiO<sub>2</sub>, WO<sub>3</sub>, and In<sub>2</sub>O<sub>3</sub> have been commonly studied for catalytic, anticancer, antibacterial, optoelectronics, and photocatalytic degradation [8–10] due to the fact of their unique physicochemical properties. Particularly, tin oxide (SnO<sub>2</sub>) NPs, an n-type semiconductor with a wide bandgap of ~3.6 eV, was studied for these purposes because of their several advantages, e.g., low cost, stability, facile synthesis, and low toxicity [11]. The hydrothermal method has been commonly used to synthesize various nanoforms of SnO<sub>2</sub> such as NPs, nanorods, and nanowires [12,13]. Earlier studies reported the photocatalytic activity of SnO<sub>2</sub> NPs under UV or visible light illumination [14,15]. However, there is a large scope for further improvement of the photocatalytic performance of such nanostructures.

Graphene is a 2D nanocrystal consisting of single layer of carbon atoms arranged in a honeycomb lattice. Graphene oxide (GO) and reduced graphene oxide (rGO) are the two most important derivatives of graphene [16,17]. GO and rGO are promising materials for various applications due to the fact of their interesting properties such as high surface area, high mechanical strength, excellent optical property, and presence of functional groups on their surfaces. Due to the presence of functional groups, GO and rGO have attracted the attention of material scientists for the synthesis of nanocomposites with metal oxide NPs [18,19]. Earlier studies focused on improving the physicochemical properties of metal oxide NPs by integration of GO or rGO [20,21]. Moreover, GO has different advantages that enhance the properties natural polymer as a nanocomposite. For example, natural polymer/GO composites (KGM/GO) are strong and biocompatible [22]. Different synthesis procedures, such as laser irradiation, gas–liquid interface interaction, co-precipitation, and hydrothermal, were employed to prepare metal oxide NPs anchored on GO/rGO nanosheets [23]. Such nanocomposites have superior characteristics than their individual one. For instance, ZnO-rGO NCs have better anticancer efficiency than pure ZnO NPs [20]. Au-rGO NCs were prepared by green synthesis for PTT of MCF7 cancer cell treatment with promising application in the field of nanobiomedicine [24]. Another study demonstrated that the photocatalytic activity of Fe<sub>3</sub>O<sub>4</sub> NPs improved after doping with rGO [25]. Chen et al. [26] reported that the prepared Pd nanocatalyst exhibited an outstanding catalytic applicability for reducing extremely poisonous Cr(VI) and a broad variety of azo dyes.

Keeping the above in mind, we aimed to improve the anticancer and photocatalytic activity of SnO<sub>2</sub> NPs by incorporating rGO. Pure SnO<sub>2</sub> NPs and SnO<sub>2</sub>-rGO NCs were produced using the one-pot hydrothermal method. X-ray diffraction (XRD), field emission scanning electron microscopy (FE-SEM), field emission transmission electron microscopy (FE-TEM), X-ray photoelectron microscopy (XPS), Raman scattering microscopy, Fourier transmission infrared (FTIR) microscopy, UV–Vis spectrometry, and photoluminescence (PL) spectrometry were applied to characterize the physicochemical properties of the prepared samples. The photocatalytic activity of SnO<sub>2</sub> NPs and SnO<sub>2</sub>-rGO NCs was examined against methylene blue (MB) dye under UV illumination. The anticancer potential of these samples were explored in two different cancer cells: human liver cancer (HepG2) and human lung cancer (A549).

## 2. Experimental Section

### 2.1. Materials and Reagents

Tine chloride (SnCl<sub>4</sub>·4H<sub>2</sub>O), graphite powder, sodium nitrate (NaNO<sub>3</sub>), sulphuric acid (H<sub>2</sub>SO<sub>4</sub>), potassium permanganate (KMnO<sub>4</sub>), hydrogen peroxide (H<sub>2</sub>O<sub>2</sub>), hydrazine monohydrate (NH<sub>2</sub>NH<sub>2</sub>·H<sub>2</sub>O), and methyl blue (MB) dye were obtained from Sigma Aldrich (Millipore-Sigma, St. Louis, MO, USA). Distilled water (DW) was employed as a medium for preparation. The chemicals were utilized as received without any further purification.

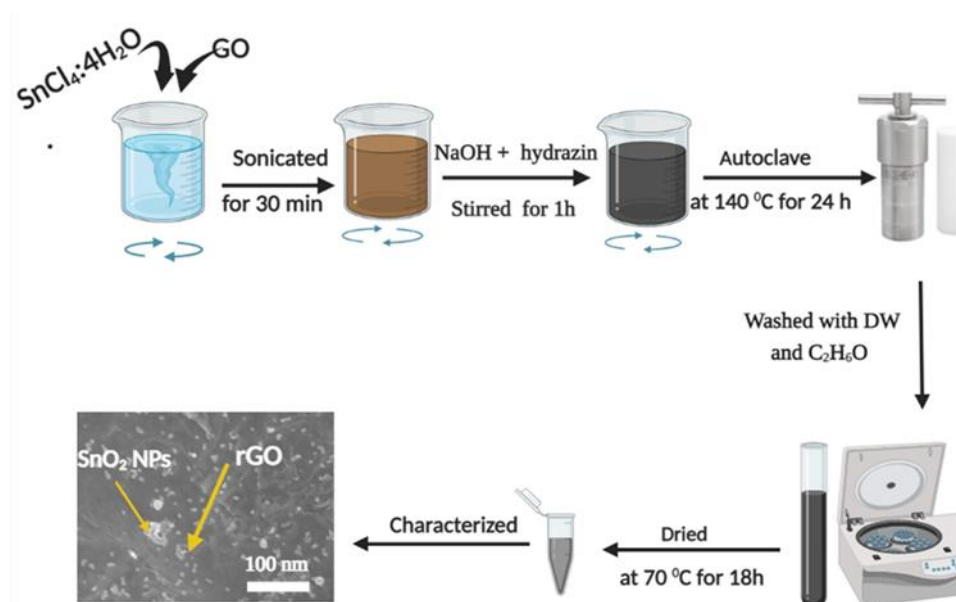
### 2.2. Synthesis of Graphene Oxide and Reduced Graphene Oxide

Graphene oxide (GO) was synthesized via Hummer's method [27]. A reduction method was used to synthesize rGO to form GO. The 200 mg of GO was dispersed in 30 mL

of DW. Then, 0.5 mL of hydrazine monohydrate ( $\text{NH}_2\text{NH}_2 \cdot \text{H}_2\text{O}$ ) was added to the above solution. The mixture solution was further warmed to  $80^\circ\text{C}$  for 3 h to reduce GO into rGO. Subsequently, the suspension was centrifuged and rinsed several times with ethanol and distilled water and finally dried at  $70^\circ\text{C}$  for 18 h to obtain the rGO sheets.

### 2.3. Synthesis of $\text{SnO}_2$ -rGO Nanocomposites

A one-pot hydrothermal approach was applied to prepare the  $\text{SnO}_2$ -rGO NCs. Briefly, 1 g of stannous chloride ( $\text{SnCl}_4 \cdot 4\text{H}_2\text{O}$ ) and 0.2 g of GO were dispersed in 30 mL of DW and sonicated for 30 min. Then, 1.5 mL of hydrazine ( $\text{NH}_2\text{NH}_2 \cdot \text{H}_2\text{O}$ ) was added to this solution. The NaOH solution was further slowly added to the mixture to reach pH 13. Next, the mixture was stirred for 1 h to obtain a homogenous solution. Fifty milliliters was transferred to a stainless autoclave and heated at  $140^\circ\text{C}$  for 24 h. After, the product was centrifuged, washed several times with ethanol and DW, and dried at  $70^\circ\text{C}$  for 18 h to obtain the  $\text{SnO}_2$ -rGO NCs. A similar procedure was applied for the synthesis of pure  $\text{SnO}_2$  NPs without mixing of GO. The synthesis protocol of the  $\text{SnO}_2$ -rGO NCs is depicted in Scheme 1.



**Scheme 1.** Synthesis protocol of the  $\text{SnO}_2$ -rGO NCs.

### 2.4. Characterization Techniques

X-ray diffraction (PanAnalytic XPert Pro, Malvern Instruments, Malvern, Worcestershire, UK), with  $\text{Cu-K}\alpha$  radiation ( $\lambda = 0.15405\text{ nm}$ , at 45 kV and 40 mA) and an angle ranging from  $30^\circ$  to  $80^\circ$ , was used to investigate the crystal structure and phase purity of the prepared samples. The morphology was studied via field emission transmission electron microscopy (FETEM) (200 kV, 2100F, JEOL, Inc., Tokyo, Japan). Mapping of the elemental distribution of the  $\text{SnO}_2$ -rGO NCs was carried out by field emission scanning electron microscopy (FE-SEM) (JSM-7600F, JEOL, Inc.). Moreover, the chemical state and elemental composition of  $\text{SnO}_2$ -rGO NCs were determined by X-ray photoelectron spectroscopy (XPS) (PHI-5300 ESCA PerkinElmer, Boston, MA, USA) and energy-dispersive X-ray spectroscopy (EDX) [28]. Moreover, the typical working conditions of XPS were  $10^{-9}$  Torr. This is necessary because the released photoelectrons have a low energy and are easily absorbed by the surrounding environment.  $\text{Al K}\alpha$  with  $\text{Mg}\alpha$  X-rays were used to excite the samples. A micro-Raman spectroscopic analysis was also performed using a Raman microscope (Thermo Scientific, Waltham, MA, USA) with a 532 nm (6 mW) laser and 32 two-second scans (IY-Horiba-T64000). The absorption spectra of the  $\text{SnO}_2$  NPs and  $\text{SnO}_2$ -rGO NCs were recorded using a UV-Visible spectrophotometer (Hitachi U-2600). The PL peak intensity of  $\text{SnO}_2$  NPs and  $\text{SnO}_2$ -rGO NCs were assessed by a fluorescent

spectrometer (Hitachi F-4600, Hitachi, Tokyo, Japan) with an excitation wavelength of 300 nm. The effect of the rGO sheets on the microstructure of the SnO<sub>2</sub> NPs was studied by Fourier transform infrared (FTIR) (PerkinElmer Paragon 500, Waltham, MA, USA).

### 2.5. Cell Culture

Human liver cancer (HepG2) and human lung cancer (A549) cell lines were used to assess the anticancer activity of NPs and NCs. Cell lines were purchased from American Type Culture Collection (ATCC, Manassas, WV, USA). Cells were cultured in DMEM (Invitrogen, Carlsbad, CA, USA) with 10% fetal bovine serum (FBS) and antibiotics (100 µg/mL streptomycin + 100 U/mL penicillin). Cells were maintained in a humidified incubator at 37 °C with a 5% CO<sub>2</sub> supply.

### 2.6. Exposure Protocol

An amount of 1000 µg/mL of both of SnO<sub>2</sub> NPs and SnO<sub>2</sub>-rGO NCs were dissolved in DMEM as stock suspension. The suspension was further diluted to different concentrations (i.e., 0, 5, 10, 25, 50, 100, and 200 µg/mL). The different dilutions NPs and NCs were sonicated for 20 min at 80 W at room temperature in an ultrasonic water bath sonicator before being exposed to cells.

### 2.7. Cell Viability

To evaluate the effect of the synthesized samples against two types of cancer (i.e., HepG2 and A549), MTT assays were performed. At a density of  $1 \times 10^4$  cells/well, 100 µL of cells were placed onto 96-well plates and incubated for 24 h. Then, 100 µL of each concentration (i.e., 0, 5, 10, 25, 50, 100, and 200 µg/mL) of the SnO<sub>2</sub> NPs and the SnO<sub>2</sub>-rGO NCs were added into each well and incubated for 24 h. After, 100 µL of MTT solution was added to each well and incubated for 3 h. Next, 100 µL of CHAPS detergent (3-(3-cholamidopropyl) (dimethylammonio)-1-propanesulfonate) solution was added into each well to solubilize the MTT dye. Cell viability was then measured using a microplate reader (BioTek ELx800 Universal) at a wavelength of 570 nm.

### 2.8. Photocatalytic Evaluation

The photocatalytic experiments were conducted through degradation of MB dye under UV illumination ( $\lambda \geq 420$  nm), which was provided using a 400 W Xe lamp (CEL-HXF300, Beijing China Education Au-light Co., Ltd., Beijing, China). The 10 ppm of MB dye was dispersed in 50 mL of DI water under continuous stirring, and 2 mL of MB solution was taken as dye without catalysts. Then, 20 mg of both of SnO<sub>2</sub> NPs and SnO<sub>2</sub>-rGO NCs was added to the above solution as a suspension solution. Before exposure to UV irradiation, an adsorption–desorption equilibrium was achieved after 30 min of stirring the suspension solution in the dark. At regular intervals, 2 mL of suspension under light was taken and centrifuged to remove the catalyst powders. The degradation efficiency of MB dye was estimated by following Equation (1).

$$\text{Degradation efficiency (\%)} = \left[ \frac{C_0 - C_t}{C_0} \right] \times 100 \quad (1)$$

where  $C_0$  represents the absorbance before irradiation, and  $C_t$  indicates the absorbance throughout the irradiation. To examine cycle stability, the catalysts were separated from suspension by centrifugation and subsequent washing with ethanol and deionized water. The catalysts were further dried at 60 °C for 12 h and utilized several times.

## 3. Results and Discussion

### 3.1. Crystallographic Study

The crystalline structure and phase formation of GO, rGO, SnO<sub>2</sub> NPs, and SnO<sub>2</sub>-rGO NCs were examined by X-ray diffraction (XRD). The XRD spectra of GO and rGO nanosheets showed  $2\theta$  values of peaks at 10.57°, 27.94°, and 24.86° corresponding to the

(001), (100), and (002) planes, respectively. In Figure 1, various  $2\theta$  (hkl) values of peaks are shown in the SnO<sub>2</sub>-rGO NCs at 26.24° (110), 33.92° (101), 37.94° (200), 51.60° (211), 58.30° (220), 61.8° (002), 78.48° (202), and 83.31° (321) planes. The results reveal that the peak of the (002) plane of graphitic carbon in the SnO<sub>2</sub>-rGO nanocomposites (NCs) overlapped with the (110) plane of the SnO<sub>2</sub> NPs [29]. All of the SnO<sub>2</sub> peaks in the XRD spectra associated to the standard SnO<sub>2</sub> (JCPDS card No: 01-0803912). The average crystalline sizes of the SnO<sub>2</sub> NPs and SnO<sub>2</sub>-rGO NCs were calculated using the Scherrer equation applying a (110) peak.

$$D = \frac{k\lambda}{\beta \cos \theta} \quad (2)$$

where  $k = 0.90$  is the shape factor of the crystallite,  $\lambda$  is the wavelength,  $\beta$  is the full width at half maximum, and  $\theta$  is the reflection angle.

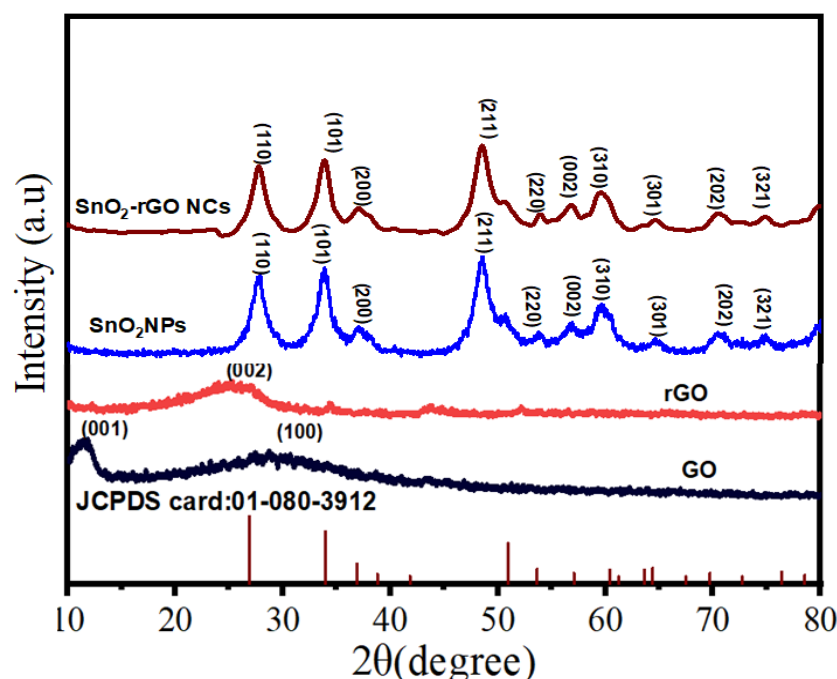


Figure 1. XRD spectra of GO, rGO, SnO<sub>2</sub> NPs, and SnO<sub>2</sub>-rGO NCs.

According to Scherrer's equation, the average crystallite size of the SnO<sub>2</sub> NPs and SnO<sub>2</sub>-rGO NCs were 7.64 and 7.98 nm, respectively (Table 1). The crystallite size of the SnO<sub>2</sub> NPs decreased after loading on rGO as shown in other reports [30,31].

Table 1. Structural and Optical Properties of the SnO<sub>2</sub> NPs and SnO<sub>2</sub>-rGO NCs.

Properties	SnO <sub>2</sub> NPs	SnO <sub>2</sub> -rGO NCs
XRD size (nm)	7.64	7.98
TEM size (nm)	9.42	9.84
Optical bandgap (eV)	3.79	3.45

### 3.2. Morphological Study

High-resolution TEM (HRTEM) images were selected to investigate the morphology, chemical compositions, and particle size of the synthesized samples (Figure 2). TEM and HRTEM images show that GO exhibited thick, flattened nanosheet-like surfaces. Navazani et al. [32] reported that the increased thickness of the graphene sheets was attributed to organic functional groups and the electrostatic interaction of oxides on the surface. TEM images (Figure 2G,H) show that the distribution of the SnO<sub>2</sub> NPs was ran-

domly agglomerated with a uniform particles size owing to smaller particle size and higher surface energy of SnO<sub>2</sub> NPs as reported earlier [33]. TEM images (Figure 2L,M) of the SnO<sub>2</sub>-rGO NCs show that the SnO<sub>2</sub> NPs were loaded onto the rGO nanosheet. These results suggest the successful formation of SnO<sub>2</sub>-rGO NCs. Figure 2I,N show that the lattice spacing (*d*) of the SnO<sub>2</sub> NPs and SnO<sub>2</sub>-rGO NCs were found to be 0.220 and 0.330 nm, respectively, which matched to the (210) and (110) planes of the SnO<sub>2</sub> structure [34,35]. These values of interplanar spacing (*d*) were supported by the XRD data.

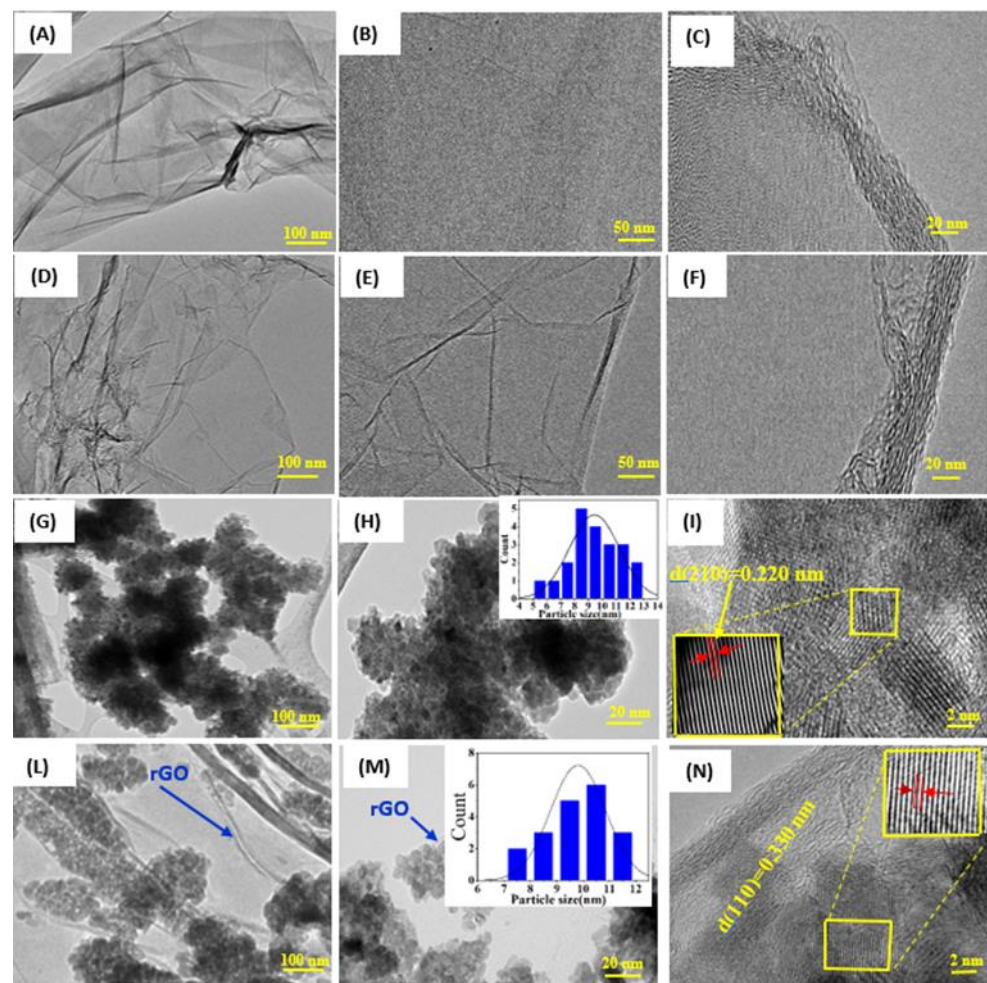


**Figure 2.** TEM characterization: TEM and HRTEM images of GO (A–C); rGO (D–F); SnO<sub>2</sub> NPs (G–I); SnO<sub>2</sub>-rGO NCs (L–N).

### 3.3. SEM Study

FE-SEM measurements were used to study the surface morphology of the prepared samples. Figure 3 displays the FE-SEM images of GO, rGO, SnO<sub>2</sub> NPs, and SnO<sub>2</sub>-rGO NCs. In Figure 3A,B, the structure of GO and rGO nanosheets can be observed as a carbon layer. Figure 3C,D shows that the SnO<sub>2</sub> NPs were spherical shaped with a uniform distribution and an anchored rGO sheet, which was also confirmed by TEM analysis. Ahamed et al. [36] observed that rGO improved the anticancer therapy of metal oxide NPs by tuning its physicochemical properties. Such a phenomenon is crucial and useful for photocatalytic degradation and cancer therapy. EDX spectra (Figure 4A) confirmed the presence of Sn, C, and O elements in the SnO<sub>2</sub>-rGO NCs. SEM mapping (Figure 4C,E) of SnO<sub>2</sub>-rGO NCs also exhibited a homogeneous distribution of Sn, O, and C elements in the SnO<sub>2</sub>-rGO NCs.

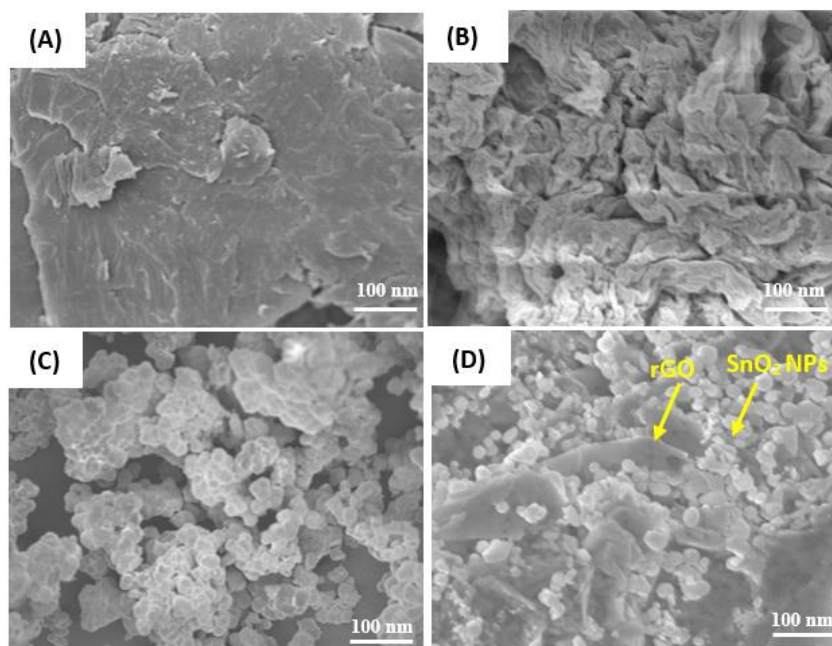


**Figure 3.** FE-SEM images of GO (A); rGO (B); SnO<sub>2</sub> NPs (C); SnO<sub>2</sub>-rGO NCs (D).

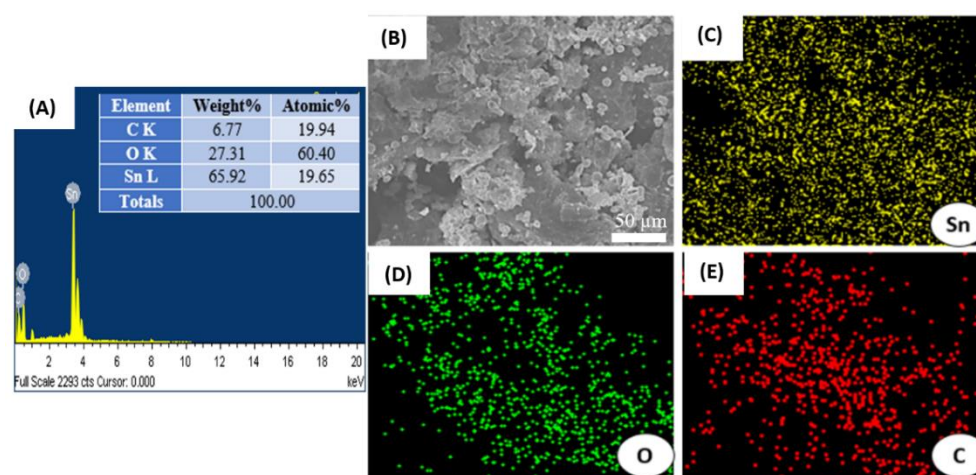


**Figure 4.** The elemental composition of the SnO<sub>2</sub>-rGO NCs by EDX (A). SEM elemental mapping of the SnO<sub>2</sub>-rGO NCs: (B) tin (Sn); (C) oxygen (O); (D); carbon (C) (E).

### 3.4. XPS Study

The electronic structure and the chemical composition of the SnO<sub>2</sub>-rGO NCs samples were also investigated by X-ray photoelectron spectroscopy (XPS), thus providing information on the electronic communication between SnO<sub>2</sub> and rGO [37]. The binding energy peaks of Sn, O, and C elements were shown in the XPS wide spectra (Figure 5A) of the SnO<sub>2</sub>-rGO NCs. It can be seen that peaks of the Sn element were matched to the spin-orbit peaks of Sn 3p, Sn 3d, and Sn 4p [38]. The high-resolution spectra of the Sn, O, and C are presented in Figure 5B–D, respectively. The results suggest that the presence of Sn, O, and C peaks confirm the fabrication of SnO<sub>2</sub> on rGO as supported by the EDX data (Figure 4A). The binding energy of the Sn3d<sub>5/2</sub> and Sn3d<sub>3/2</sub> peaks were assigned at 486.55 and 495.3 eV, respectively, which could be attributed to the SnO<sub>2</sub> NPs [39]. According to the curve fit of the O1s spectra (Figure 5C), the binding energy peaks of O1s at 532 and 533 eV corresponded to Sn-O and Sn-O-C, respectively, which agrees with previous works [40,41]. The C1s peak (Figure 5D) was subdivided into three individual peaks after the fitting of the main peak. The peaks at 284, 285, and 288 eV were observed to correspond to C=C, C-OH,

and O-C=O, respectively, as shown in a previous study [42]. These results reveal that the rGO had a residual oxygen group [40].

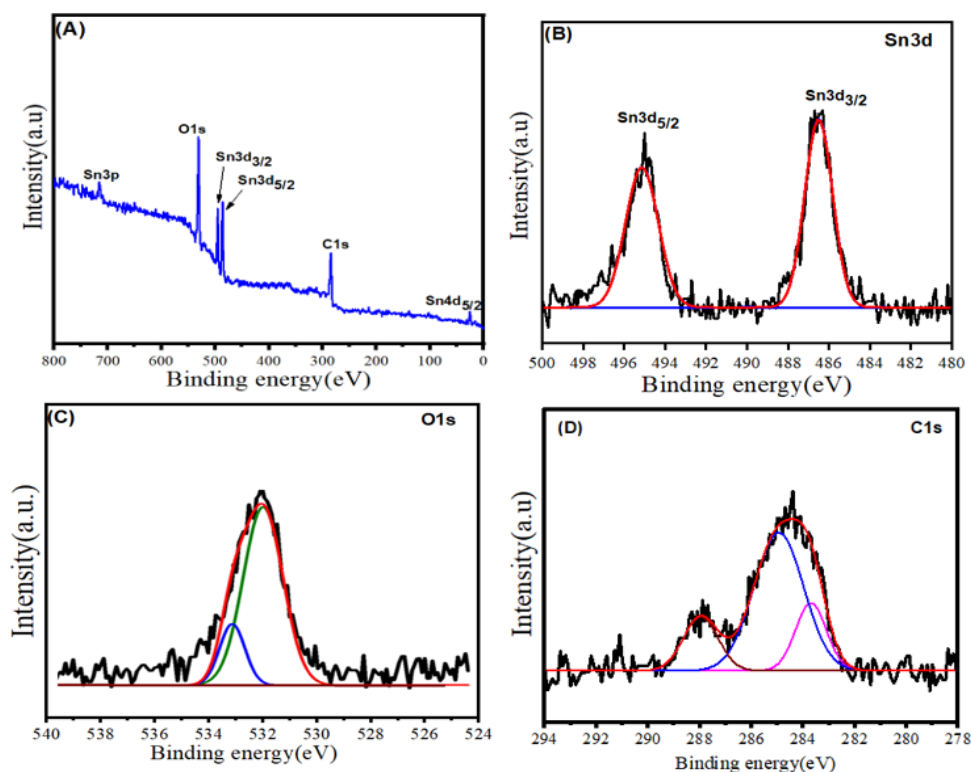


**Figure 5.** XPS wide spectra of SnO<sub>2</sub>-rGO NCs (A); Sn3d high-resolution XPS spectra (B); O1s high-resolution XPS spectra (C); C1s high-resolution XPS spectra (D).

### 3.5. Raman Analysis

The electronic and vibration bands of prepared samples were analyzed via Raman spectroscopy. The Raman spectra of the SnO<sub>2</sub> NPs and SnO<sub>2</sub>-rGO NCs are shown in Figure 6A. It can be seen that E<sub>u</sub>, A<sub>g</sub>, A<sub>1g</sub>, and B<sub>2g</sub> vibration bands of the SnO<sub>2</sub> NPs' peaks were located at 352.33, 579, 620, and 773.32 cm<sup>-1</sup>, respectively [43]. The peak positions at 579 and 620 cm<sup>-1</sup> of the SnO<sub>2</sub>-rGO NCs were similar to the SnO<sub>2</sub> NPs as shown in Figure 6A. These results indicate that the intensity of the Raman peaks of the SnO<sub>2</sub>-rGO NCs was lower than the SnO<sub>2</sub> NPs due to the interaction between SnO<sub>2</sub> NPs and rGO [39]. Figure 6B shows that two new scattering bands (i.e., band D and band G) appeared in the SnO<sub>2</sub>-rGO NCs compared to the SnO<sub>2</sub> NPs. Moreover, the scattering bands of the SnO<sub>2</sub>-rGO NCs were observed at 1349.47 cm<sup>-1</sup> (band D) and 1590.50 cm<sup>-1</sup> (band G), which were attributed to instability in the hexagonal graphitic layers and vibration bonds of the carbon atom, respectively [44]. Our results from the Raman analysis confirm that the SnO<sub>2</sub> NPs attached onto the surface of the rGO sheets [45].

### 3.6. FTIR Study

The functional groups of the GO, rGO, SnO<sub>2</sub> NPs, and SnO<sub>2</sub>-rGO NCs were determined by FTIR spectrometry. Figure 7 shows the FTIR spectra of the prepared samples in a range of 450–4000 cm<sup>-1</sup>. The results reveal the changes in the microstructural characteristics in the first region (500–650 cm<sup>-1</sup>) of the SnO<sub>2</sub> NPs during loading on rGO. However, three stretching vibrations of C-O, C=C, and C=O assigned at 1048.73, 1620, and 1734.92 cm<sup>-1</sup>, respectively, can be seen in the GO. The presence of C=O and C-O at the 1713.96 and 1048.37 cm<sup>-1</sup> bands indicate the reduction of GO into rGO [46]. Moreover, O-H stretching vibrations were observed at 3433.69, 1646.43, and 1353 cm<sup>-1</sup> for both SnO<sub>2</sub> NPs and SnO<sub>2</sub>-rGO NCs due to the existence water molecules during the hydrothermal



process [47]. The band observed at  $593\text{ cm}^{-1}$  was assigned to the O-Sn-O stretching mode in the SnO<sub>2</sub> NPs [48], while two strong peaks at  $530.20$  and  $608.6\text{ cm}^{-1}$  in the SnO<sub>2</sub>-rGO NCs were assigned to Sn-O stretching vibration owing to the strong interaction between SnO<sub>2</sub> and rGO [49]. These results indicate the formation of single-structure SnO<sub>2</sub>-rGO NCs as supported by the XRD data.

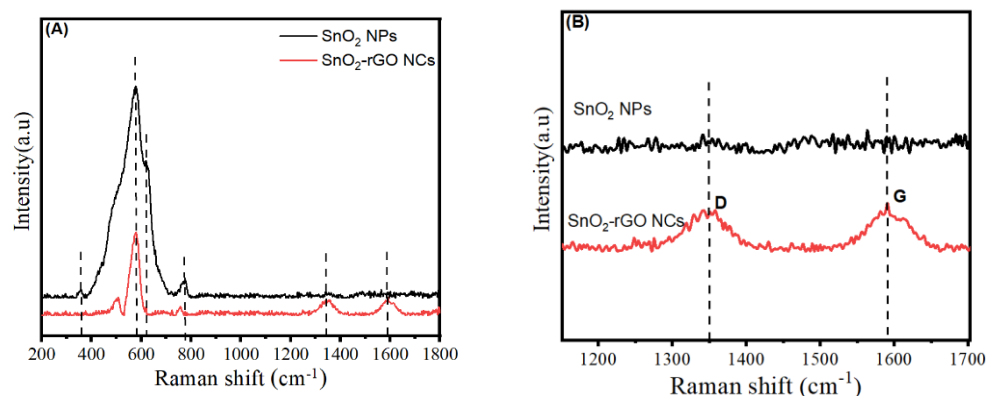


**Figure 6.** Raman spectra of the SnO<sub>2</sub> NPs and SnO<sub>2</sub>-rGO NCs (A); magnified Raman spectra of the SnO<sub>2</sub> NPs and SnO<sub>2</sub>-rGO NCs (B).

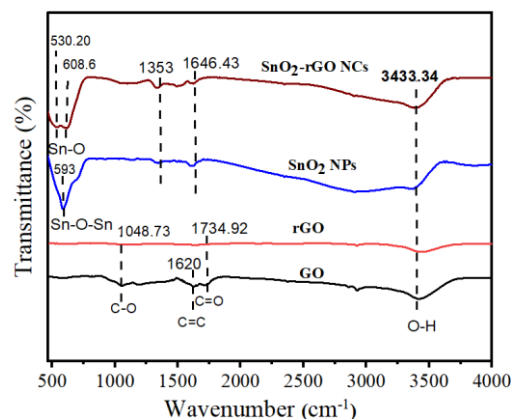


**Figure 7.** FTIR spectra of the prepared GO, rGO, SnO<sub>2</sub> NPs, and SnO<sub>2</sub>-rGO NCs.

### 3.7. Optical Study

The optical properties of the SnO<sub>2</sub> NPs and SnO<sub>2</sub>-rGO NCs were studied by UV-Vis spectroscopy. The UV-Vis spectra of the SnO<sub>2</sub> NPs and SnO<sub>2</sub>-rGO NCs are presented in Figure 8A. The absorption edge was shifted toward a higher wavelength for the SnO<sub>2</sub>-rGO NCs in comparison to pure SnO<sub>2</sub> NPs. The difference in absorption peaks tuned the bandgap energy of the SnO<sub>2</sub>-rGO NCs in comparison to the SnO<sub>2</sub> NPs. Taucs formula was used to assess the bandgap energy [50]. The bandgap energy ( $E_g$ ) (Figure 8B) of the SnO<sub>2</sub> NPs and SnO<sub>2</sub>-rGO NCs were 3.79 and 3.45 eV, respectively. We observed a slight decrease in the bandgap energy of the SnO<sub>2</sub> NPs after rGO integration due to the increase in particle size as shown Table 1. Reduction of the bandgap energy improves UV light absorption, which can be applied in the photocatalytic degradation of pollutants [51].

### 3.8. Photoluminescence (PL)

Photoluminescence (PL) was used to measure the migration rate of electrons and holes in the SnO<sub>2</sub>NPs and SnO<sub>2</sub>-rGO NCs NPs. The PL spectra of the SnO<sub>2</sub>NPs and SnO<sub>2</sub>-rGO NCs NPs are presented in Figure 9. Moreover, the PL spectra of the SnO<sub>2</sub> NPs and SnO<sub>2</sub>-rGO NCs at room temperature were obtained using an excitation wavelength of 355 nm. After adding rGO, an emission peak at 402 nm was greatly reduced. Our results

observed that the PL intensity of the SnO<sub>2</sub>-GO NCs system (black line) was lower than that of pure SnO<sub>2</sub> NPs, which may be attributed to greater charge separation, a longer life of the electron–hole pair, and a higher efficiency of charge [52]. This process has the potential to be used in a large variety of applications including cancer treatment and the photocatalytic degradation of environmental contaminants.

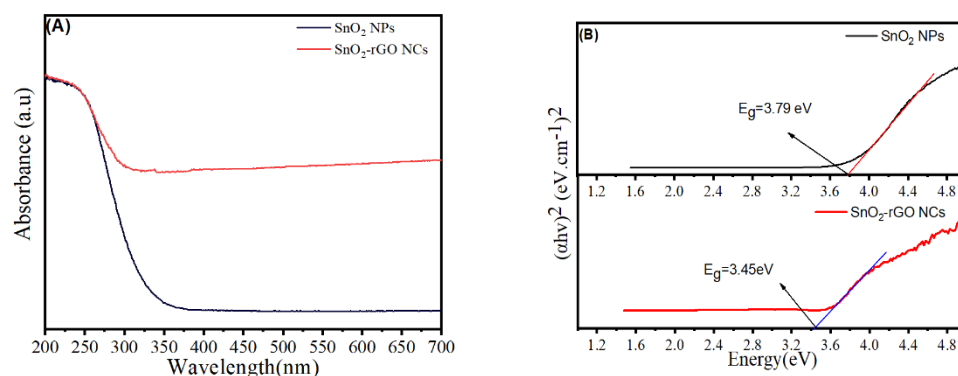


**Figure 8.** UV–Vis spectra of the SnO<sub>2</sub>NPs and SnO<sub>2</sub>-rGO NCs (A); the bandgap energy of the SnO<sub>2</sub> NPs and SnO<sub>2</sub>-rGO NCs (B).

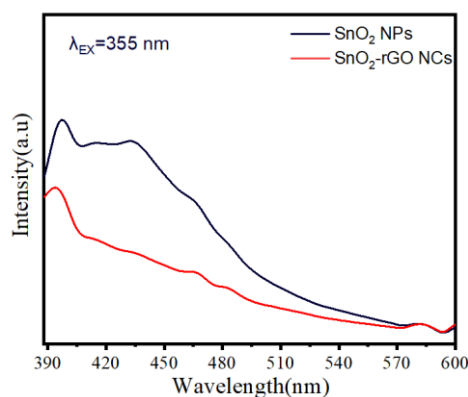


**Figure 9.** PL spectra of the SnO<sub>2</sub>NPs and SnO<sub>2</sub>-rGO NCs.

### 3.9. Photocatalytic Study

The degradation of MB dye under UV irradiation was used to investigate the photocatalytic activity of the SnO<sub>2</sub> NPs and SnO<sub>2</sub>-rGO NCs. Figure 10A,B shows the absorption spectra of the MB solution of the SnO<sub>2</sub> NPs and SnO<sub>2</sub>-rGO NCs under UV irradiation within 50 min. The absorption wavelength of the MB solution was at 664 nm as shown in Figure 10. We observed that the intensity of the absorption at 664 nm in the MB spectra decreased with increasing exposure time. Additionally, the color of the MB solution faded gradually, indicating the breaking of the dye’s structure by oxidation [53]. Ali et al. [54] also observed that MB dye was degraded by nanocomposites (NCs) under UV irradiation over a short exposure time.

Figure 11A depicts the variations in ( $C_t/C_0$ ) as a function of exposure time for pure SnO<sub>2</sub> NPs and SnO<sub>2</sub>-rGO NCs at different time intervals (0–50 min) under UV irradiation. The photocatalytic activity of the nanocomposites was enhanced by rGO integration [55]. The results show that the degradation efficiency of the SnO<sub>2</sub>-rGO NCs (93%) under UV light after 50 min was higher than for the SnO<sub>2</sub> NPs (54%). The reaction kinetics of the current catalysis can be described as pseudo-first-order kinetics, i.e.,  $\ln(C_t/C_0) = -kt$  ( $k$  = kinetic rate constant,  $t$  = reaction time,  $C_0$  = initial absorbance, and  $C_t$  = absorbance at time  $t$ ). The rate constant ( $K$ ) values of the SnO<sub>2</sub> NPs and SnO<sub>2</sub>-rGO NCs were 0.0231 and 0.0102 min<sup>−1</sup>, respectively (Figure 11B). Figure 11D displays the recyclability of the SnO<sub>2</sub>-rGO NCs after a four-time run with the same experimental conditions. The catalysts were

washed in ethanol and deionized water and centrifuged to test for cycle stability. Then, catalysts were dried at 60 °C for 12 h and used multiple times. Even after four runs, the degradation efficiency of the MB dye was still approximately 93%. This indicates that the photocatalytic performance of the SnO<sub>2</sub>-rGO NCs can be continuously used without damage during the oxidation of contaminants. Our results indicate that the SnO<sub>2</sub>-rGO NCs had outstanding stability and potential for application in environmental remediation [56]. A comparison of the present samples' degradation efficiency of MB dye with previous studies is shown in Table 2.

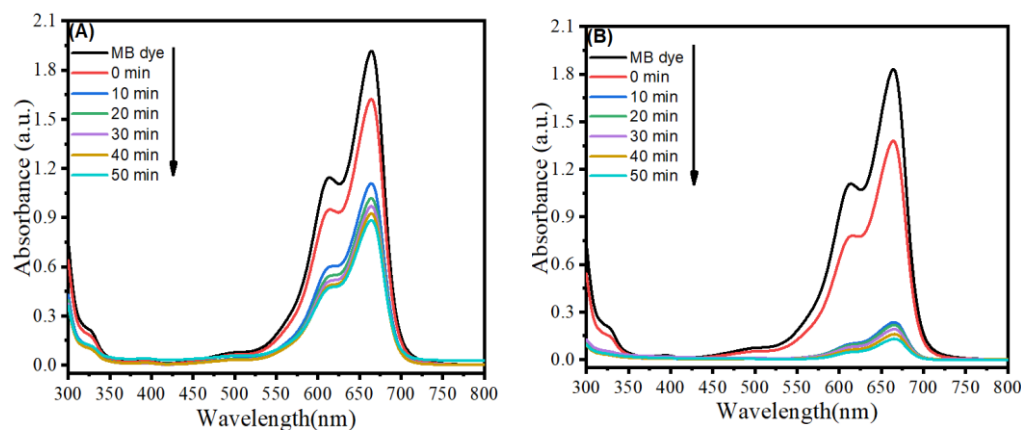


Figure 10. UV-Vis absorbance spectra for the degradation of the MB dye at different time intervals under UV irradiation: SnO<sub>2</sub> NPs (A); SnO<sub>2</sub>-rGO NCs (B).

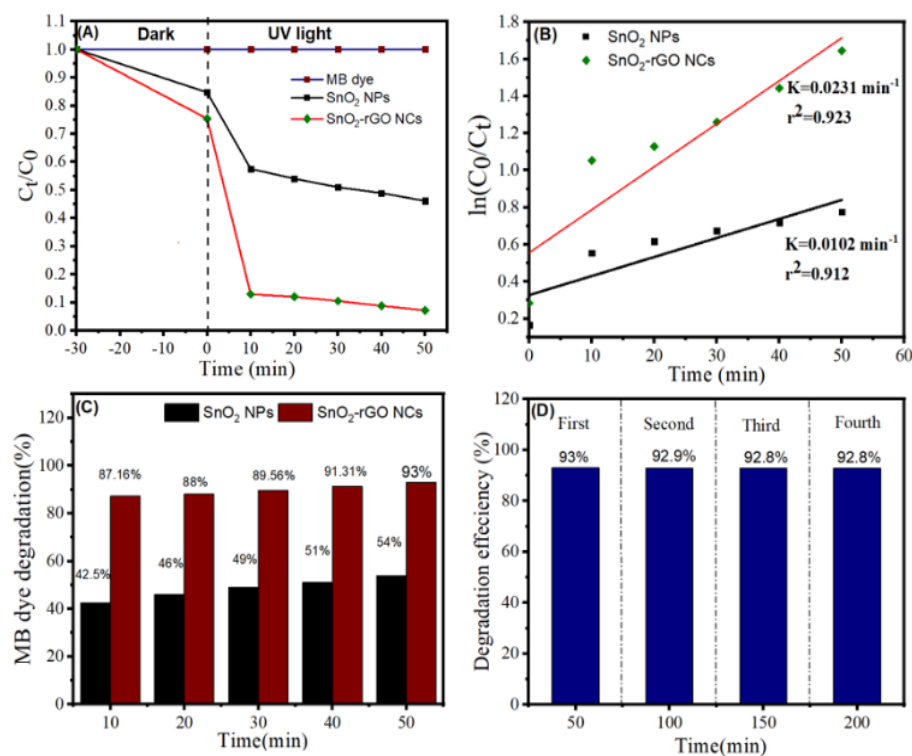


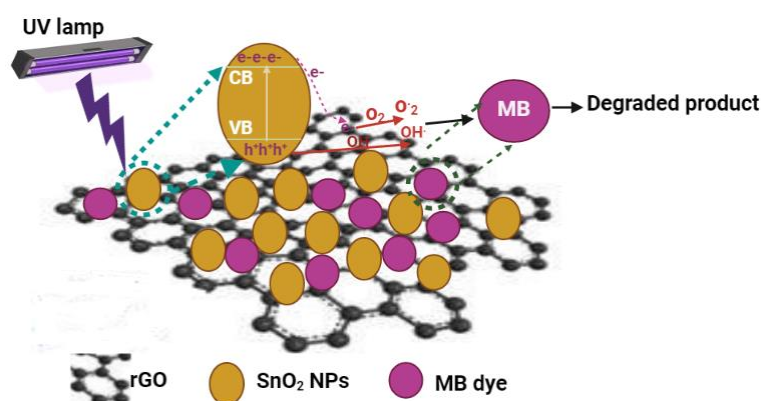
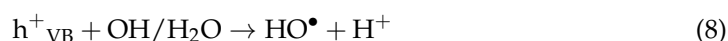
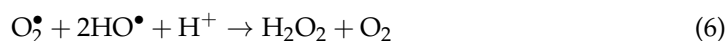
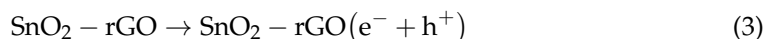
Figure 11. Variations in  $(C_t/C_0)$  as a function of irradiation time for SnO<sub>2</sub> NPs and SnO<sub>2</sub>-rGO NCs (A), The plot of  $\ln(C_0/C_t)$  as a function of light exposure time (B), the degradation efficiency of the SnO<sub>2</sub> NPs and SnO<sub>2</sub>-rGO NCs (C), and four cycling runs of the SnO<sub>2</sub>-rGO NCs for the degradation of the MB dye under UV irradiation (D).

**Table 2.** Comparison of the MB dye degradation efficiency of the present samples with previous studies.

Sample	Model Dye Pollutant	Reaction Time	Degradation Efficiency (%)	Concentration of MB	Source of Light	Reference
SnO <sub>2</sub> -rGO NCs	Methylene blue (MB)	50 min	93%	10 ppm	UV irradiation	This work
ZnO/GONCs	Methylene blue (MB)	40 min	100%	10 ppm	Sunlight irradiation	[57]
TiO <sub>2</sub> /rGO/Ag NCs	Methylene blue (MB)	120 min	91.2%	10 ppm	UV irradiation	[58]
rGO/ZnO/Cu	Methylene blue (MB)	60 min	95.14%	5 ppm	Sunlight irradiation	[59]
BiOBr/rGO NCs	Methylene blue (MB)	75 min	96%	7 ppm	Sunlight irradiation	[60]
Au/WO <sub>2.72</sub> /rGONCs	Methylene blue (MB)	60 min	91.2%	10 ppm	Sunlight irradiation	[61]

### 3.10. Mechanism of Photocatalysis

The photocatalytic mechanism for the degradation of MB dye by SnO<sub>2</sub>-rGO NCs is shown in Figure 12. The MB dye degradation process occurs via a series of chemical reactions, which generate superoxide and hydroxyl radicals. Prepared samples (SnO<sub>2</sub> NPs and SnO<sub>2</sub>-rGO NCs) and MB dye were exposed under UV radiation ( $\lambda < 400$  nm). Upon irradiating the SnO<sub>2</sub>, excited electrons in the valance band (VB) transferred to the conduction band (CB), producing holes in the VB (Equation (3)). The electrons in the CB of the SnO<sub>2</sub> NPs could transfer to the rGO due to the SnO<sub>2</sub> NPs attached to the rGO surfaces (Equation (4)). The generated electrons ( $e^-$ ) and holes ( $h^+$ ) reacted with water (H<sub>2</sub>O) to produce new free oxygen radicals (Equation (5)). These radicals can be transferred to the hydroxyl radicals (Equations (6) and (7)). Hydroxyl radicals were produced by water molecules and holes (Equation (8)). These free oxygen radicals can decompose MB dye into smaller molecules (Equation (9)). The rGO reduced the rate of electron–hole pair recombination in SnO<sub>2</sub>-rGO NCs, which further increased the degradation efficiency of the SnO<sub>2</sub>-rGO NCs.

**Figure 12.** Photocatalytic mechanism for the degradation of MB dye by the SnO<sub>2</sub>-rGO NCs.

### 3.11. Anticancer Study

Several recent studies showed that the anticancer potential of metal oxide NPs can be enhanced by integration with graphene derivatives [62,63]. For instance, Ahamed et al. [36] observed that SnO<sub>2</sub>-ZnO-rGO NCs displayed higher cytotoxicity toward human breast

cancer cells (MCF-7) in comparison to pure ZnO NPs to improve their physiochemical properties such as the bandgap energy, which was lower compared to SnO<sub>2</sub>-ZnO NPs and pure ZnO NPs. In this work, we focused on improving the cytotoxicity of SnO<sub>2</sub> NPs against cancer cells by rGO incorporation. The cytotoxicity at different concentrations (5–200 µg/mL) of SnO<sub>2</sub> NPs and SnO<sub>2</sub>-rGO NCs was assessed in human liver cancer (HepG2) and lung cancer (A549) cells (Figure 13A,B). The results indicate that both SnO<sub>2</sub> NPs and SnO<sub>2</sub>-rGO NCs induced dose-dependent cytotoxicity in the two types of cancer cells. Moreover, the SnO<sub>2</sub>-rGO NCs exerted a higher cytotoxicity than the pure SnO<sub>2</sub> NPs, and the anticancer potential of the SnO<sub>2</sub> NPs increased with rGO doping. The IC<sub>50</sub> values of the SnO<sub>2</sub>-rGO NCs were almost 1.5-fold higher in both cancer cells than for pure SnO<sub>2</sub> NPs (Table 3). These results indicate that rGO integration effectively enhanced the anticancer efficacy of the SnO<sub>2</sub> NPs. In addition, these data warrant further research on the anticancer potential of SnO<sub>2</sub>-rGO NCs in suitable in vivo models.

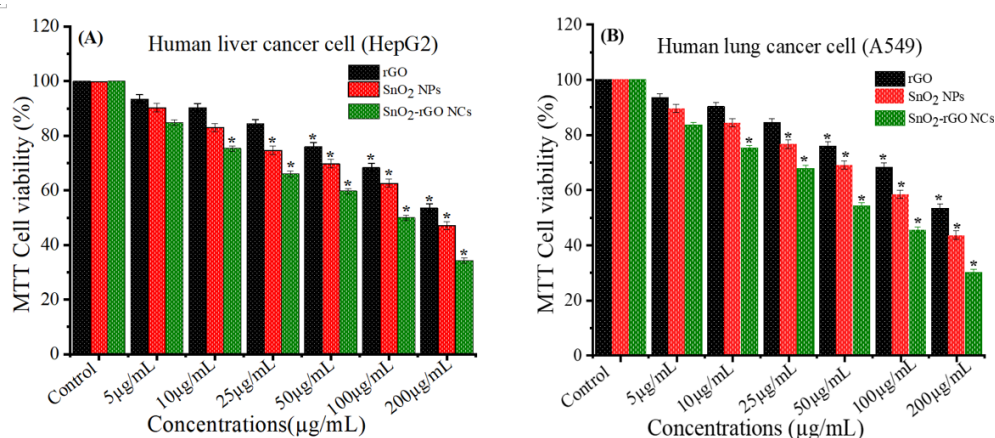


**Figure 13.** Cytotoxicity of rGO, SnO<sub>2</sub> NPs, and SnO<sub>2</sub>-rGO NCs in human liver cancer HepG2 cells (A) and lung cancer A549 cells (B); one-way ANOVA followed by the post hoc test was applied for statistical analysis. \*  $p < 0.05$ , statistically significant difference when compared to the control group.

**Table 3.** IC<sub>50</sub> values of SnO<sub>2</sub> NPs and SnO<sub>2</sub>-rGO NCs for two types of human cancer cells.

Samples	Human Liver Cancer (HepG2) Cells	Human Lung Cancer (A549) Cells
SnO <sub>2</sub> NPs	160.97 µg/mL	153.13 µg/mL
SnO <sub>2</sub> -rGO NCs	100 µg/mL	95.72 µg/mL

#### 4. Conclusions

In summary, SnO<sub>2</sub> NPs and SnO<sub>2</sub>-rGO NCs were successfully prepared using a novel one-pot hydrothermal approach. The XRD data showed that the average crystallite size of the SnO<sub>2</sub> NPs decreased after rGO doping. HRTEM and SEM results revealed that SnO<sub>2</sub> NPs tightly anchored the rGO sheets, and SnO<sub>2</sub> and rGO were uniformly distributed in the SnO<sub>2</sub>-rGO NCs with high-quality lattice fringes without distortion. The XPS and EDX data confirmed the chemical state and elemental composition of the SnO<sub>2</sub>-rGO NCs. Optical data suggested that the bandgap energy of the SnO<sub>2</sub>-rGO NCs was slightly lower than that of the pure SnO<sub>2</sub> NPs. The intensity of the PL spectra was lower in the SnO<sub>2</sub>-rGO NCs in comparison to the pure SnO<sub>2</sub> NPs. In the photocatalytic test, the MB degradation efficiency of the SnO<sub>2</sub>-rGO NCs (93%) was higher than for the SnO<sub>2</sub> NPs (54%). This can be explained by a lower bandgap energy and lower PL intensity, which reduced the separation of charge carriers (i.e., electrons and holes). Moreover, the anticancer efficacy of SnO<sub>2</sub>-rGO NCs was almost 1.5-fold higher against human liver cancer HepG2 and lung cancer A549 cells in comparison to pure SnO<sub>2</sub> NPs. These data suggest a novel approach to enhance the photocatalytic activity and anticancer performance of SnO<sub>2</sub> NPs via rGO fusion. This study

warrants further research on SnO<sub>2</sub>-rGO NCs for the photocatalytic degradation of different pollutants and anticancer efficacy in various cancer and normal cells.

**Author Contributions:** Conceptualization, M.A.; investigation and methodology, Z.M.A., H.A.A., S.A., M.J.A. and M.A.; writing—original draft preparation, Z.M.A. and M.A.; writing—review and editing, Z.M.A., H.A.A., S.A. and M.A. All authors have read and agreed to the published version of the manuscript.

**Funding:** The authors extend their sincere appreciation to the researchers who supported project number: RSP-2021/129, King Saud University, Riyadh, Saudi Arabia, for funding this research.

**Institutional Review Board Statement:** Not applicable.

**Informed Consent Statement:** Not applicable.

**Data Availability Statement:** The data presented in this study are available on request from the corresponding author.

**Conflicts of Interest:** The authors declare no conflict of interest.

## References

1. Bray, F.; Ferlay, J.; Soerjomataram, I.; Siegel, R.L.; Torre, L.A.; Jemal, A. Global cancer statistics 2018: GLOBOCAN estimates of incidence and mortality worldwide for 36 cancers in 185 countries. *CA Cancer J. Clin.* **2018**, *68*, 394–424. [[CrossRef](#)] [[PubMed](#)]
2. Ahamed, M.; Akhtar, M.J.; Khan, M.A.M.; Alhadlaq, H.A. Enhanced anticancer performance of eco-friendly-prepared Mo-ZnO/RGO nanocomposites: Role of oxidative stress and apoptosis. *ACS Omega* **2022**, *7*, 7103–7115. [[CrossRef](#)] [[PubMed](#)]
3. Giofrè, S.V.; Tiecco, M.; Celesti, C.; Patanè, S.; Triolo, C.; Gulino, A.; Spitaleri, L.; Scalese, S.; Scuderi, M.; Iannazzo, D. Eco-friendly 1,3-dipolar cycloaddition reactions on graphene quantum dots in natural deep eutectic solvent. *Nanomaterials* **2020**, *10*, 2549. [[CrossRef](#)] [[PubMed](#)]
4. Huang, L.; Sun, Y.; Mahmud, S.; Liu, H. Biological and environmental applications of silver nanoparticles synthesized using the aqueous extract of ginkgo biloba leaf. *J. Inorg. Organomet. Polym. Mater.* **2020**, *30*, 1653–1668. [[CrossRef](#)]
5. Liu, Y.; Huang, L.; Mahmud, S.; Liu, H. Gold nanoparticles biosynthesized using ginkgo biloba leaf aqueous extract for the decolorization of azo-dyes and fluorescent detection of Cr(VI). *J. Clust. Sci.* **2020**, *31*, 549–560. [[CrossRef](#)]
6. Singh, M.P.; Sirohi, P.; Afzal, S. Biosynthesis zinc oxide nanoparticles using senna occidentalis leaf extract and evaluation of their cytotoxic effect on SW480 colon cancer cell line. *Res. Sq.* **2022**, 1–20. [[CrossRef](#)]
7. Spitaleri, L.; Nicotra, G.; Zimbone, M.; Contino, A.; Maccarrone, G.; Alberti, A.; Gulino, A. Fast and efficient sun light photocatalytic activity of Au-ZnO core-shell nanoparticles prepared by a one-pot synthesis. *ACS Omega* **2019**, *4*, 15061–15066. [[CrossRef](#)]
8. Sharma, D.K.; Shukla, S.; Sharma, K.K.; Kumar, V. A Review on ZnO: Fundamental properties and applications. *Mater. Today Proc.* **2020**, *49*, 3028–3035. [[CrossRef](#)]
9. Liu, X.; Zhai, H.; Wang, P.; Zhang, Q.; Wang, Z.; Liu, Y.; Dai, Y.; Huang, B.; Qin, X.; Zhang, X. Synthesis of a WO<sub>3</sub> photocatalyst with high photocatalytic activity and stability using synergetic internal Fe<sup>3+</sup> doping and superficial Pt loading for ethylene degradation under visible-light irradiation. *Catal. Sci. Technol.* **2019**, *9*, 652–658. [[CrossRef](#)]
10. Zeng, J.; Wu, M.; Lan, S.; Li, J.; Zhang, X.; Liu, J.; Liu, X.; Wei, Z.; Zeng, Y. Facile preparation of biocompatible Ti<sub>2</sub>O<sub>3</sub> nanoparticles for second near-infrared window photothermal therapy. *J. Mater. Chem. B* **2018**, *6*, 7889–7897. [[CrossRef](#)]
11. Kar, A.; Olszówka, J.; Sain, S.; Sloman, S.R.I.; Montes, O.; Fernández, A.; Pradhan, S.K.; Wheatley, A.E.H. Morphological effects on the photocatalytic properties of SnO<sub>2</sub> nanostructures. *J. Alloys Compd.* **2019**, *810*, 151718. [[CrossRef](#)]
12. Firooz, A.A.; Mahjoub, A.R.; Khodadadi, A.A. Preparation of SnO<sub>2</sub> nanoparticles and nanorods by using a hydrothermal method at low temperature. *Mater. Lett.* **2008**, *62*, 1789–1792. [[CrossRef](#)]
13. Li, Y.; Guo, Y.; Tan, R.; Cui, P.; Li, Y.; Song, W. Synthesis of SnO<sub>2</sub> nano-sheets by a template-free hydrothermal method. *Mater. Lett.* **2009**, *63*, 2085–2088. [[CrossRef](#)]
14. Viet, P.V.; Thi, C.M.; Hieu, L. Van the high photocatalytic activity of SnO<sub>2</sub> nanoparticles synthesized by hydrothermal method. *J. Nanomater.* **2016**, *2016*, 4231046. [[CrossRef](#)]
15. Kim, S.P.; Choi, M.Y.; Choi, H.C. Photocatalytic activity of SnO<sub>2</sub> nanoparticles in methylene blue degradation. *Mater. Res. Bull.* **2016**, *74*, 85–89. [[CrossRef](#)]
16. Shams, M.; Guiney, L.M.; Huang, L.; Ramesh, M.; Yang, X.; Hersam, M.C.; Chowdhury, I. Environmental science nano paper influence of functional groups on the degradation of graphene oxide nanomaterials. *Environ. Sci. Nano* **2019**, *6*, 2203. [[CrossRef](#)]
17. Shyamala, R.; Gomathi Devi, L. Reduced graphene oxide/SnO<sub>2</sub> nanocomposites for the photocatalytic degradation of rhodamine B: Preparation, characterization, photosensitization, vectorial charge transfer mechanism and identification of reaction intermediates. *Chem. Phys. Lett.* **2020**, *748*, 137385. [[CrossRef](#)]
18. Balsamo, S.A.; Fiorenza, R.; Condorelli, M.; Pecoraro, R.; Brundo, M.V.; Lo Presti, F.; Sciré, S. One-pot synthesis of TiO<sub>2</sub>-rGO photocatalysts for the degradation of groundwater pollutants. *Materials* **2021**, *14*, 5938. [[CrossRef](#)]

19. Raslan, A.; Saenz del Burgo, L.; Ciriza, J.; Luis Pedraz, J. Graphene oxide and reduced graphene oxide-based scaffolds in regenerative medicine. *Int. J. Pharm.* **2020**, *580*, 119226. [[CrossRef](#)]
20. Ahamed, M.; Javed Akhtar, M.; Majeed Khan, M.A.; Alhadlaq, H.A. Facile green synthesis of ZnO-RGO nanocomposites with enhanced anticancer efficacy. *Methods* **2022**, *199*, 28–36. [[CrossRef](#)]
21. Zhu, J.; Zhu, T.; Zhou, X.; Zhang, Y.; Lou, X.W.; Chen, X.; Zhang, H.; Hng, H.H.; Yan, Q. Facile Synthesis of Metal Oxide/Reduced Graphene Oxide Hybrids with High Lithium Storage Capacity and Stable Cyclability. *Nanoscale* **2011**, *3*, 1084–1089. [[CrossRef](#)] [[PubMed](#)]
22. Zhu, W.K.; Cong, H.P.; Yao, H.B.; Mao, L.B.; Asiri, A.M.; Alamry, K.A.; Marwani, H.M.; Yu, S.H. Bioinspired, ultrastrong, highly biocompatible, and bioactive natural polymer/graphene oxide nanocomposite films. *Small* **2015**, *11*, 4298–4302. [[CrossRef](#)] [[PubMed](#)]
23. Hoon Suh, D.; Park, S.K.; Nakhanivej, P.; Kang, S.W.; Park, H.S. Microwave synthesis of SnO<sub>2</sub> nanocrystals decorated on the layer-by-layer reduced graphene oxide for an application into lithium ion battery anode. *J. Alloys Compd.* **2017**, *702*, 636–643. [[CrossRef](#)]
24. Yousefimehr, F.; Jafarirad, S.; Salehi, R.; Zakerhamidi, M.S. Facile fabricating of RGO and Au/RGO nanocomposites using *Brassica oleracea* var. *gongylodes* biomass for non-invasive approach in cancer therapy. *Sci. Rep.* **2021**, *11*, 11900. [[CrossRef](#)] [[PubMed](#)]
25. Khan, M.A.M.; Khan, W.; Ahamed, M.; Alhazaa, A.N. Investigation on the structure and physical properties of Fe<sub>3</sub>O<sub>4</sub>/RGO nanocomposites and their photocatalytic application. *Mater. Sci. Semicond. Process.* **2019**, *99*, 44–53. [[CrossRef](#)]
26. Chen, J.; Wei, D.; Liu, L.; Nai, J.; Liu, Y.; Xiong, Y.; Peng, J.; Mahmud, S.; Liu, H. Green synthesis of konjac glucomannan templated palladium nanoparticles for catalytic reduction of Azo compounds and hexavalent chromium. *Mater. Chem. Phys.* **2021**, *267*, 124651. [[CrossRef](#)]
27. Bansode, S.R.; Khare, R.T.; Jagtap, K.K.; More, M.A.; Koinkar, P. One step hydrothermal synthesis of SnO<sub>2</sub>-RGO nanocomposite and its field emission studies. *Mater. Sci. Semicond. Process.* **2017**, *63*, 90–96. [[CrossRef](#)]
28. Matthew, J. *Surface Analysis by Auger and X-Ray Photoelectron Spectroscopy*; Briggs, D., Grant, J.T., Eds.; IMPublications: Chichester, UK; SurfaceSpectra: Manchester, UK, 2003; ISBN 1-901019-04-7.
29. Nurzulaikha, R.; Lim, H.N.; Harrison, I.; Lim, S.S.; Pandikumar, A.; Huang, N.M.; Lim, S.P.; Thien, G.S.H.; Yusoff, N.; Ibrahim, I. Graphene/SnO<sub>2</sub> nanocomposite-modified electrode for electrochemical detection of dopamine. *Sens. Bio-Sens. Res.* **2015**, *5*, 42–49. [[CrossRef](#)]
30. Pham, V.T.; le Trung, H.; Tran, N.K.; Chu Manh, H.; Nguyen Duc, H.; Tran Thi Quynh, H.; Pham, T.H. Hydrothermal synthesis, structure, and photocatalytic properties of SnO<sub>2</sub>/RGO nanocomposites with different GO concentrations. *Mater. Res. Express* **2018**, *5*, 095506. [[CrossRef](#)]
31. Priyadharsan, A.; Vasanthakumar, V.; Karthikeyan, S.; Raj, V.; Shanavas, S.; Anbarasan, P.M. Multi-functional properties of ternary CeO<sub>2</sub>/SnO<sub>2</sub>/RGO nanocomposites: Visible light driven photocatalyst and heavy metal removal. *J. Photochem. Photobiol. A Chem.* **2017**, *346*, 32–45. [[CrossRef](#)]
32. Navazani, S.; Shokuhfar, A.; Hassanisadi, M.; Askarieh, M.; Di Carlo, A.; Agresti, A. Facile synthesis of a SnO<sub>2</sub>@rGO nanohybrid and optimization of its methane-sensing parameters. *Talanta* **2018**, *181*, 422–430. [[CrossRef](#)] [[PubMed](#)]
33. Drzymała, E.; Gruzeł, G.; Depciuch, J.; Budziak, A.; Kowal, A.; Parlinska-Wojtan, M. Structural, chemical and optical properties of SnO<sub>2</sub> NPs obtained by three different synthesis routes. *J. Phys. Chem. Solids* **2017**, *107*, 100–107. [[CrossRef](#)]
34. Ahmad, S.; Ahmad, A.; Khan, S.; Ahmad, S.; Khan, I.; Zada, S.; Fu, P. Algal extracts based biogenic synthesis of reduced graphene oxides (RGO) with enhanced heavy metals adsorption capability. *J. Ind. Eng. Chem.* **2019**, *72*, 117–124. [[CrossRef](#)]
35. Zhang, B.; Zhang, C.; Liu, B.; Zhou, X.; Huang, G. Anchoring Sb<sub>2</sub>O<sub>3</sub>/SnO<sub>2</sub> nano-heterojunction on reduced graphene oxide as lithium ion batteries anodes with remarkable rate performance and excellent cycle stability. *Ionics* **2021**, *27*, 4205–4216. [[CrossRef](#)]
36. Ahamed, M.; Akhtar, M.J.; Khan, M.A.M.; Alhadlaq, H.A. SnO<sub>2</sub>-doped ZnO/reduced graphene oxide nanocomposites: Synthesis, characterization, and improved anticancer activity via oxidative stress pathway. *Int. J. Nanomed.* **2021**, *16*, 89–104. [[CrossRef](#)]
37. Gulino, A. Structural and electronic characterization of self-assembled molecular nanoarchitectures by X-ray photoelectron spectroscopy. *Anal. Bioanal. Chem.* **2013**, *405*, 1479–1495. [[CrossRef](#)]
38. Tian, R.; Zhang, Y.; Chen, Z.; Duan, H.; Xu, B.; Guo, Y.; Kang, H.; Li, H.; Liu, H. The effect of annealing on a 3D SnO<sub>2</sub>/graphene foam as an advanced lithium-ion battery anode. *Sci. Rep.* **2016**, *6*, 19195. [[CrossRef](#)]
39. Pi, S.; Zhang, X.; Cui, H.; Chen, D.; Zhang, G.; Xiao, S.; Tang, J. Facile fabrication of Au nanoparticles/Tin oxide/reduced graphene oxide ternary nanocomposite and its high-performance SF<sub>6</sub> decomposition components sensing. *Front. Chem.* **2019**, *7*, 476. [[CrossRef](#)]
40. Al-Gaashani, R.; Najjar, A.; Zakaria, Y.; Mansour, S.; Atieh, M.A. XPS and structural studies of high quality graphene oxide and reduced graphene oxide prepared by different chemical oxidation methods. *Ceram. Int.* **2019**, *45*, 14439–14448. [[CrossRef](#)]
41. Jiang, S.; Huang, R.; Zhu, W.; Li, X.; Zhao, Y.; Gao, Z.; Gao, L.; Zhao, J. Free-standing SnO<sub>2</sub>@rGO anode via the anti-solvent-assisted precipitation for superior lithium storage performance. *Front. Chem.* **2019**, *7*, 878. [[CrossRef](#)]
42. Bhangare, B.; Rangir, N.S.; Jagtap, S.; Debnath, A.K.; Muthe, K.P.; Terashima, C.; Aswal, D.K.; Gosavi, S.W.; Fujishima, A. XPS and kelvin probe studies of SnO<sub>2</sub>/RGO nanohybrids based NO<sub>2</sub> sensors. *Appl. Surf. Sci.* **2019**, *487*, 918–929. [[CrossRef](#)]
43. Wang, X.; Wang, X.; Di, Q.; Zhao, H.; Liang, B.; Yang, J. Mutual effects of fluorine dopant and oxygen vacancies on structural and luminescence characteristics of F doped SnO<sub>2</sub> nanoparticles. *Materials* **2017**, *10*, 1398. [[CrossRef](#)] [[PubMed](#)]

44. Rahimi, A.; Kazeminezhad, I.; Mousavi Ghahfarokhi, S.E. Synthesis and investigation of SnS<sub>2</sub>/RGO nanocomposites with different GO concentrations: Structure and optical properties, photocatalytic performance. *J. Mater. Sci. Mater. Electron.* **2018**, *29*, 4449–4456. [[CrossRef](#)]
45. Du, F.; Yang, B.; Zuo, X.; Li, G. Dye-sensitized solar cells based on low-cost nanoscale SnO<sub>2</sub>@RGO composite counter electrode. *Mater. Lett.* **2015**, *158*, 424–427. [[CrossRef](#)]
46. Akada, K.; Terasawa, T.O.; Imamura, G.; Obata, S.; Saiki, K. Control of work function of graphene by plasma assisted nitrogen doping. *Appl. Phys. Lett.* **2014**, *104*, 131602. [[CrossRef](#)]
47. Khan, M.A.M.; Khan, W.; Ahamed, M.; Ahmed, J.; Al-Gawati, M.A.; Alhazaa, A.N. Silver-decorated cobalt ferrite nanoparticles anchored onto the graphene sheets as electrode materials for electrochemical and photocatalytic applications. *ACS Omega* **2020**, *5*, 31076–31084. [[CrossRef](#)] [[PubMed](#)]
48. Wang, Y.; Ding, J.; Liu, Y.; Liu, Y.; Cai, Q.; Zhang, J. SnO<sub>2</sub>@reduced graphene oxide composite for high performance lithium-ion battery. *Ceram. Int.* **2015**, *41*, 15145–15152. [[CrossRef](#)]
49. Guo, W.; Zhou, Q.; Zhang, J.; Fu, M.; Radacsi, N.; Li, Y. Hydrothermal synthesis of Bi-Doped SnO<sub>2</sub>/RGO nanocomposites and the enhanced gas sensing performance to benzene. *Sens. Actuators B Chem.* **2019**, *299*, 126959. [[CrossRef](#)]
50. Orek, C.; Gündüz, B.; Kaygili, O.; Bulut, N. Electronic, optical, and spectroscopic analysis of TBADN organic semiconductor: Experiment and theory. *Chem. Phys. Lett.* **2017**, *678*, 130–138. [[CrossRef](#)]
51. Mani, R.; Vivekanandan, K.; Subiramaniyam, N.P. Photocatalytic activity of different organic dyes by using pure and Fe doped SnO<sub>2</sub> nanopowders catalyst under UV light irradiation. *J. Mater. Sci. Mater. Electron.* **2017**, *28*, 13846–13852. [[CrossRef](#)]
52. Van Tuan, P.; Tuong, H.B.; Tan, V.T.; Thu, L.H.; Khoang, N.D.; Khiem, T.N. SnO<sub>2</sub>/reduced graphene oxide nanocomposites for highly efficient photocatalytic degradation of methylene blue. *Opt. Mater.* **2022**, *123*, 111916. [[CrossRef](#)]
53. Sujatmiko, F.; Sahroni, I.; Fadillah, G.; Fatimah, I. Visible light-responsive photocatalyst of SnO<sub>2</sub>/RGO prepared using pometia pinnata leaf extract. *Open Chem.* **2021**, *19*, 174–183. [[CrossRef](#)]
54. Ali, G.; Zaidi, S.J.A.; Abdul Basit, M.; Park, T.J. Synergetic performance of systematically designed G-C<sub>3</sub>N<sub>4</sub>/RGO/SnO<sub>2</sub> nanocomposite for photodegradation of rhodamine-B dye. *Appl. Surf. Sci.* **2021**, *570*, 151140. [[CrossRef](#)]
55. Gomari, N.; Kazeminezhad, I.; Ghahfarokhi, S.E.M. Impact of morphology evolution of ZnSn(OH)<sub>6</sub> microcubes on photocatalytic activity of ZnSn(OH)<sub>6</sub>/SnO<sub>2</sub>/RGO ternary nanocomposites for efficient degradation of organic pollutants. *Opt. Mater.* **2021**, *113*, 110878. [[CrossRef](#)]
56. Nenavathu, B.P.; Kandula, S.; Verma, S. Visible-light-driven photocatalytic degradation of safranin-T dye using functionalized graphene oxide nanosheet (FGS)/ZnO nanocomposites. *RSC Adv.* **2018**, *8*, 19659–19667. [[CrossRef](#)]
57. Al-Rawashdeh, N.A.F.; Allabadi, O.; Aljarrah, M.T. Photocatalytic activity of graphene oxide/zinc oxide nanocomposites with embedded metal nanoparticles for the degradation of organic dyes. *ACS Omega* **2020**, *5*, 28046–28055. [[CrossRef](#)]
58. Tian, H.; Wan, C.; Xue, X.; Hu, X.; Wang, X. Effective electron transfer pathway of the ternary TiO<sub>2</sub>/RGO/Ag nanocomposite with enhanced photocatalytic activity under visible light. *Catalysts* **2017**, *7*. [[CrossRef](#)]
59. Asgharian, M.; Mehdipourghazi, M.; Khoshandam, B.; Keramati, N. Photocatalytic degradation of methylene blue with synthesized RGO/ZnO/Cu. *Chem. Phys. Lett.* **2019**, *719*, 1–7. [[CrossRef](#)]
60. Shih, K.-Y.; Kuan, Y.-L.; Wang, E.-R. One-step microwave-assisted synthesis and visible-light photocatalytic activity enhancement of BiOBr/RGO nanocomposites for degradation of methylene blue. *Materials* **2021**, *14*, 4577. [[CrossRef](#)]
61. Li, B.; Shao, X.; Liu, T.; Shao, L.; Zhang, B. Construction of metal/WO<sub>2.72</sub>/RGO ternary nanocomposites with optimized adsorption, photocatalytic and photoelectrochemical properties. *Appl. Catal. B Environ.* **2016**, *198*, 325–333. [[CrossRef](#)]
62. Tammina, S.K.; Mandal, B.K.; Ranjan, S.; Dasgupta, N. Cytotoxicity study of piper nigrum seed mediated synthesized SnO<sub>2</sub> nanoparticles towards colorectal (HCT116) and lung cancer (A549) cell lines. *J. Photochem. Photobiol. B Biol.* **2017**, *166*, 158–168. [[CrossRef](#)] [[PubMed](#)]
63. Ahamed, M.; Akhtar, M.J.; Khan, M.A.M.; Alaizeri, Z.A.M.; Alhadlaq, H.A. Evaluation of the cytotoxicity and oxidative stress response of CeO<sub>2</sub>-RGO nanocomposites in human lung epithelial A549 cells. *Nanomaterials* **2019**, *9*, 1709. [[CrossRef](#)] [[PubMed](#)]